Cell Reports
Physical Science

CellPress
OPEN ACCESS

Article

Complete Reconstruction of Hydrate Pre-Catalysts for Ultrastable Water Electrolysis in Industrial-Concentration Alkali Media

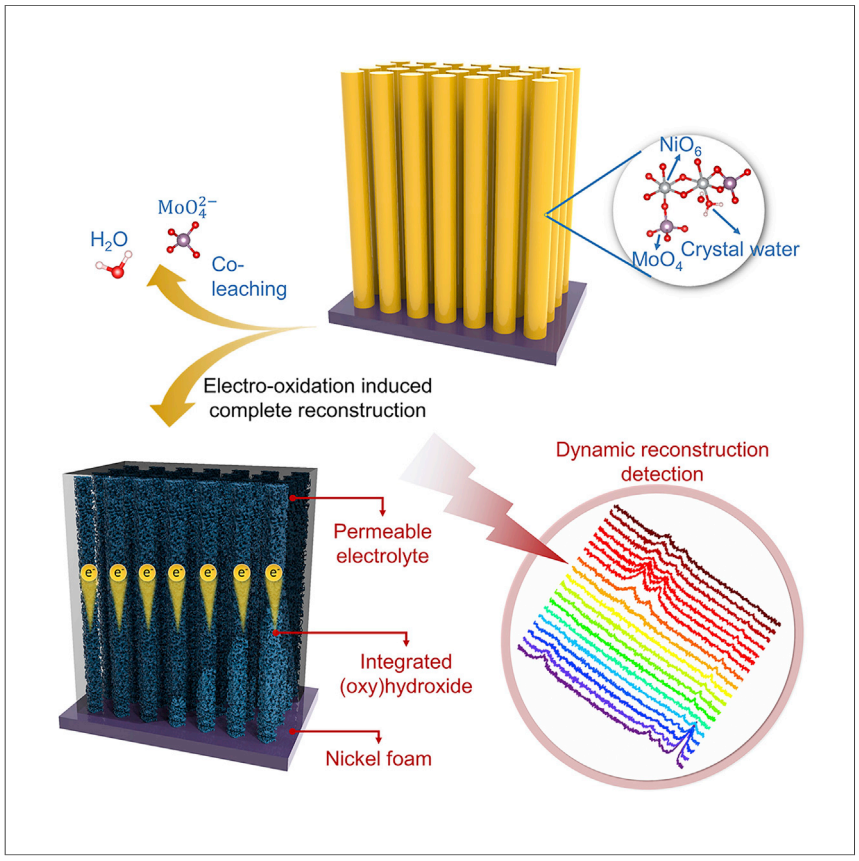

Fundamental investigations of the reconstruction of pre-catalysts and evaluation of their performance under realistic conditions are vital to promote practical applications. Liu et al. study the dynamic reconstruction, including geometric/phase structure, of hydrate molybdates at oxidized potentials. They highlight that reconstruction engineering toward completely reconstructed catalysts leads to materials that are active and stable under industrial conditions.

Xiong Liu, Jiashen Meng, Kun Ni, ..., Xiaojun Wu, Liqiang Mai, Dongyuan Zhao

wujs@whut.edu.cn (J.W.)
mlq518@whut.edu.cn (L.M.)

HIGHLIGHTS

Electro-oxidation induces complete reconstruction on hydrate molybdate pre-catalyst

The key to complete reconstruction is a loose reconstruction layer

Microstructure of completely reconstructed material provides ultrastable catalyst

Performance evaluation of water electrolysis under realistic conditions

Liu et al., Cell Reports Physical Science 1, 100241
November 18, 2020
https://doi.org/10.1016/j.xcrp.2020.100241

Cell Reports
Physical Science

CellPress
OPEN ACCESS

Article

Complete Reconstruction of Hydrate Pre-Catalysts for Ultrastable Water Electrolysis in Industrial-Concentration Alkali Media

Xiong Liu,[1,5] Jiashen Meng,[1,5] Kun Ni,[3,5] Ruiting Guo,[1] Fanjie Xia,[1] Jingjing Xie,[1] Xu Li,[1] Bo Wen,[1] Peijie Wu,[1] Ming Li,[1] Jinsong Wu,[1,*] Xiaojun Wu,[3] Liqiang Mai,[1,2,6,*] and Dongyuan Zhao[1,4]

SUMMARY

Fundamental investigations of reconstruction of oxygen evolution reaction (OER) pre-catalysts and performance evaluation under realistic conditions are vital for practical water electrolysis. Here, we capture dynamic reconstruction, including the geometric/phase structure, of hydrate molybdates at oxidized potentials. Etching-reconstruction engineering endows the formed NiOOH with a sub-5-nm particle-interconnected structure, as revealed by multi-angle electron tomography. The key to complete reconstruction is the multicomponent co-leaching-induced loose reconstruction layer, conductive to solution penetration and mass transport. This unique structure avoids particle agglomeration in catalysis and promotes complete exploitation of the catalyst with 1,350 h of durability to meet industrial requirements. Upon addition of iron during reconstruction, mainstream Fe-NiOOH with a retained structure forms. Coupled with MoO_2-Ni arrays in a membrane-free and two-electrode cell, it achieves stable electrolysis in industrial-concentration KOH for 260 h. This work highlights the reconstruction chemistry of hydrate oxygen-evolving systems and their performance evaluation under industrial conditions.

INTRODUCTION

The oxygen evolution reaction (OER) is pivotal because of its multiple prospective energy storage devices, including water electrolyzers and rechargeable metal-air batteries;[1–4] however, the OER pathways are complex and generally impose significant kinetic bottlenecks with large overpotentials (usually more than 350 mV).[5] The benchmark Ru/Ir catalysts can hardly satisfy scaled up practical utilization because of their scarcity, prohibitive cost, and detrimental environmental effects.[6] Nowadays, earth-abundant transition-metal-based compounds have comparable performance and, thus, have attracted extensive attention as alternatives.[7–9] However, most of these compounds undergo surface reconstruction under operating conditions, which makes it difficult to capture the dynamic structure and recognize real catalyst information.[10] For example, Ni-based OER electrocatalysts,[11,12] such as chalcogenides, nitrides, and phosphides, are thermodynamically less stable than oxides in strongly oxidative environments. The electro-derived oxidation on their surface induces reconstruction to form target OER-active oxides/(oxy)hydroxides (Table S1), which have been identified as real active species.[13] These post-OER catalysts generally show a near-surface reconstruction structure at the nanoscale, such as a core-shell structure, containing a large percentage of inactive atoms in the core.[14] Because of their limited near-surface reaction region,[15,16] the evolving catalysts

[1]State Key Laboratory of Advanced Technology for Materials Synthesis and Processing, Wuhan University of Technology, Wuhan 430070, Hubei, China

[2]Foshan Xianhu Laboratory of the Advanced Energy Science and Technology Guangdong Laboratory, Xianhu Hydrogen Valley, Foshan 528200, China

[3]Hefei National Laboratory for Physical Sciences at the Microscale, School of Chemistry and Materials Sciences, CAS Key Laboratory of Materials for Energy Conversion, CAS Center for Excellence in Nanoscience, iChEM (Collaborative Innovation Center of Chemistry for Energy Materials), University of Science and Technology of China, Hefei, Anhui 230026, China

[4]Department of Chemistry, State Key Laboratory of Molecular Engineering of Polymers, Shanghai Key Laboratory of Molecular Catalysis and Innovative Materials, iChEM, Fudan University, Shanghai 200433, China

[5]These authors contributed equally

[6]Lead Contact

*Correspondence: wujs@whut.edu.cn (J.W.), mlq518@whut.edu.cn (L.M.)

https://doi.org/10.1016/j.xcrp.2020.100241

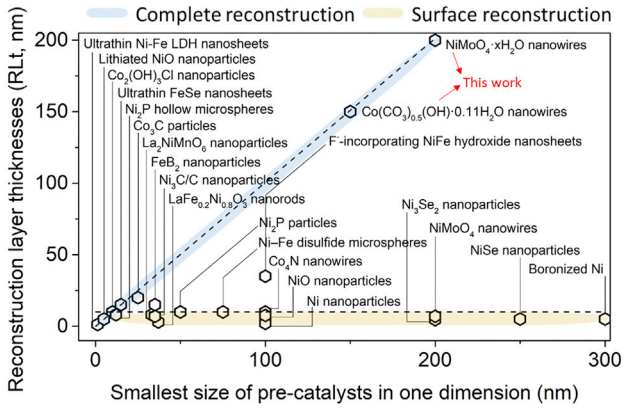

Figure 1. Summary of Reconstruction Results

Shown are reconstruction layer thicknesses (RLts) and the smallest size of OER pre-catalysts in one dimension in this work and previous reports.

usually exhibit incompletely developed catalytic activity. The compositional complexity of partially reconstructed catalysts greatly hinders an insightful understanding of catalytic origins.[17] Therefore, it raises curiosity and challenges in fundamental mechanistic research of the reconstruction chemistry of pre-catalysts, including origins of limited reconstruction degrees and dynamic reconstruction mechanisms.

The reconstruction results of reconstruction layer thickness (RLt) and the smallest size in one dimension based on reported OER pre-catalysts are summarized in Figure 1 (see also Table S2). The RLt values for most reported pre-catalysts are less than 10 nm. Deep/complete reconstruction will maximize the number of active sites in reconstructed catalysts and thus endow high-mass-activity catalysis. To date, very few studies have focused on completely reconstructed (CR) catalysts.[18–20] Because of the fast reconstruction processes, deep comprehension of reconstruction is crucial but difficult. Despite its importance, the general synthesis method and underlying mechanism of CR catalysts have not been reported. More importantly, most current reports investigate catalyst performance in low-concentration alkali (0.1–1 M KOH) rather than in industrial-concentration 20–30 wt % KOH.[18–21] Harsh conditions may result in different reconstruction results for pre-catalysts. Evaluating catalysts in 20–30 wt % KOH for alkaline water electrolysis (AWE) can promote their commercial application.[22] Therefore, it is meaningful for performance evaluation under realistic operating conditions.

As illustrated in Schemes 1A–1C, we present etching-leaching-reconstruction engineering to achieve complete reconstruction of bulk hydrate pre-catalysts. As a proof of concept, various *in/ex situ* technologies were employed to capture the time-resolved structural/phase evolution of $NiMoO_4 \cdot xH_2O$ under electro-oxidation conditions. The reconstruction steps generally consist of complete collapse of hydrates with co-leaching of crystal water and MoO_4^{2-} and then its reconstruction to NiOOH via electro-oxidation. Intrinsically, the loose reconstruction layer caused by co-leaching is the key to promote deep penetration of solution and, thus, complete reconstruction. However, for $NiMoO_4$, the entire crystal structure could not be disintegrated by alkali etching, and the formed dense layer prevents electrolyte penetration for further etching and/or reconstruction. Therefore, the formed, partially reconstructed $NiMoO_4$@NiOOH features an inert core part because of

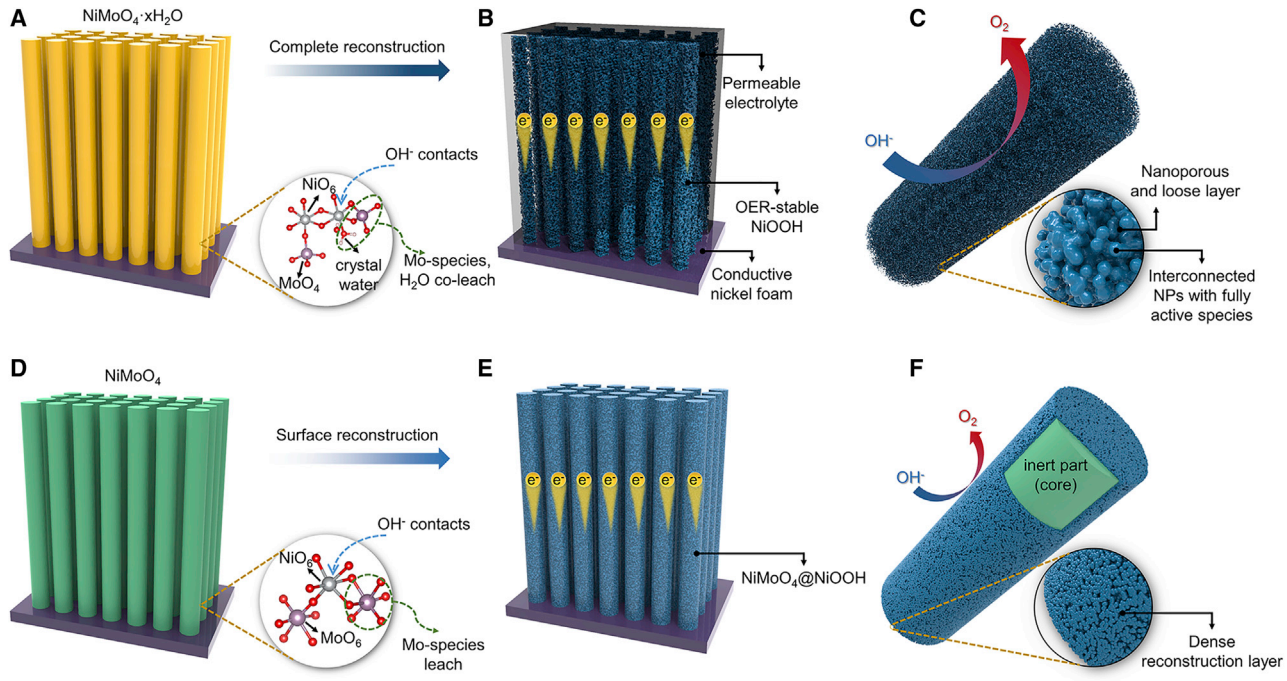

Scheme 1. Complete/Surface Reconstruction Diagram

(A–C) Etching-leaching-reconstruction engineering achieves complete reconstruction of $NiMoO_4 \cdot xH_2O$, forming an ultrasmall NP-interconnected multilevel structure. During dynamic reconstruction, its self-instability in alkali forms oxide with nanopores created by co-leaching of crystal water and soluble Mo species. Simultaneously, the oxide evolves to high-valence Ni^{3+} species at oxidized potentials. The formed loose reconstruction layer is pivotal to trigger full diffusion of electrolytes into inner parts for complete reconstruction.

(D–F) Surface reconstruction of $NiMoO_4$ to form core-shell $NiMoO_4$@NiOOH, with the low reconstruction degree limited by a dense reconstruction layer.

near-surface catalysis properties (Schemes 1D–1F). More importantly, the unique interconnected structure of CR catalysts endows them with ultrastable catalysis and potential AWE applications under realistic conditions.

RESULTS AND DISCUSSION

Morphological/Phase Evolution

$NiMoO_4 \cdot xH_2O$ nanowires (NWs) grown on conductive nickel foam (NF) were fabricated using a low-temperature hydrothermal method that has demonstrated manufacturing amplification capability (>250 cm^2 in one-pot synthesis) toward commercial applications (Figure S1). These nanowires are monocrystalline with a smooth surface, confirmed by transmission electron microscopy (TEM) imaging and the corresponding selected area electron diffraction (SAED) pattern (Figure S2). Its crystal structure was determined via atomic substitution and structure optimization because the powder X-ray diffraction (XRD) pattern is similar to that of the reported analog $CoMoO_4 \cdot 0.75H_2O$.[23] The loss of lattice water (LW) does not induce collapse of the $NiMoO_4 \cdot xH_2O$ framework, and the obvious phase evolution occurs when the calcination temperature is higher than 400°C, which is attributed to loss of coordination water (CW) (Figure S3).Nickel foam cannot maintain its flexibility and toughness for direct non-binder catalysis when heated to more than 600°C. Therefore, a proper calcination temperature of 550°C was chosen to fabricate the anhydrous $NiMoO_4$ nanowire arrays.

Cyclic voltammetry (CV) activation was conducted at 0.924–1.724 V versus reversible hydrogen electrode (V_{RHE}), resulting in two different geometric/phase

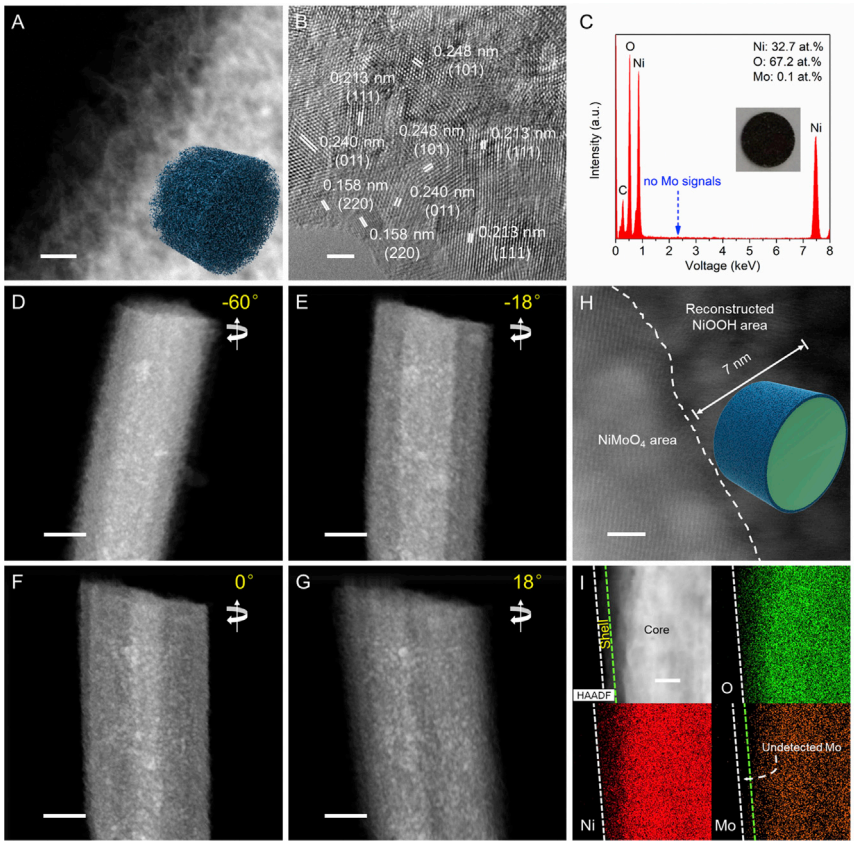

Figure 2. Different Reconstruction Results for $NiMoO_4 \cdot xH_2O$ and $NiMoO_4$

(A and B) (A) HAADF-STEM and (B) HRTEM images of CR-NiOOH. Scale bars, 10 and 2 nm, respectively. The inset in (A) shows a schematic diagram of CR-NiOOH.

(C) EDX spectrum of CR-NiOOH. Inset: optical photo of black CR-NiOOH/NF.

(D–G) Representative HAADF-STEM images captured from a multi-angle electron tomography video of a single CR-NiOOH nanowire. Scale bars, 50 nm.

(H and I) HAADF-STEM image of $NiMoO_4$@NiOOH and (I) the corresponding elemental mapping. Scale bars, 2 and 20 nm, respectively. The inset in (H) shows a schematic diagram of $NiMoO_4$@NiOOH.

structures of $NiMoO_4 \cdot xH_2O$ and $NiMoO_4$. For $NiMoO_4 \cdot xH_2O$, CR-NiOOH forms in a stable state during OER (Figure S4). High-angle annular dark-field scanning TEM (HAADF-STEM) imaging clearly demonstrates its morphological characterization, which is represented schematically in an inset in Figure 2A. Such a nanowire is interconnected by sub-5-nm ultrasmall nanoparticles (NPs), resulting in visible interspaces with ~5-nm nanopores accessible to electrolytes. All interplanar spacings of NPs within the nanowire are well indexed to the planes of NiOOH (Figure 2B). The exposed interplanar spacings of 0.158, 0.208, 0.213, 0.240, and 0.248 nm can be well assigned to the (220), (210), (111), (011), and (101) planes of orthorhombic NiOOH (Joint Committee on Powder Diffraction Standards [JCPDS] 27-956), respectively. It displays low-crystalline and polycrystalline characteristics confirmed by the SAED pattern (Figure S4D). Only two Raman peaks at 474 and 554 cm^{-1} belonging to the e_g bending and the A_{1g} stretching vibration of Ni-O in NiOOH[24] are observed (Figure S4E), and the O/Ni atomic ratio is 2.05 from the corresponding energy-dispersive X-ray (EDX) spectroscopy spectrum (Figure 2C), which further demonstrates the pure phase of CR-NiOOH. In addition, negligible content (0.1 atomic percentage [at.%]) of the Mo element suggests its absence within the

nanowire. The color of CR-NiOOH is black (inset in Figure 2C), which is the typical color of nickel (oxy)hydroxide. Tomographic data were further analyzed to show its three-dimensional structure from multiple perspectives (Figures 2D–2G; Video S1). Electron tomography was conducted at consecutive rotational angles from −60° to 48°, and HAADF-STEM images were collected simultaneously. High homogeneity of ultrasmall NPs and no agglomerated large particles are observed from various rotational angles. Particularly, CR catalysts that featured an ultrasmall NP-interconnected structure with evenly distributed gas-permeable pores were reported first.

Different from $NiMoO_4 \cdot xH_2O$, $NiMoO_4$ undergoes surface reconstruction occurs after 1-day continuous electro-oxidation, which results in core-shell $NiMoO_4$@NiOOH nanowires. Only an ~7-nm-thick NiOOH layer forms, and the inner continuous lattice fringes covering dozens of nanometers are indexed to the planes of $NiMoO_4$ (JCPDS 86-0361) (Figure 2H; Figures S5A and S5B). STEM element mapping further confirms the core-shell structure as undetected Mo signals in the shell region (Figure 2I). No diffraction signals are assigned to NiOOH from the SAED pattern (Figure S5C), and Raman spectra of $NiMoO_4$ before and after activation remain almost unchanged (Figure S5D). The undetected Raman/SAED signals of NiOOH are attributed to its ultrathin layer structure. The reported Ni-Mo nitride after activation also occurred the partial reconstruction just like $NiMoO_4$.[25]

Identification of Dynamic Reconstruction Processes

Ex situ high-resolution TEM (HRTEM) characterizations during potential-controlled CV measurements were carried out to uncover the morphological evolution of $NiMoO_4 \cdot xH_2O$. An ~2.66-fold current density at 1.724 V_{RHE} is achieved when comparing the 20^{th} cycle with the initial one, with the area of the closed curves increasing gradually (Figure 3A). Only 20 cycles with 640-s duration are required to achieve complete reconstruction, indicating a fast reconstruction rate. The redox peak currents are gradually stabilized in the 15^{th}–20^{th} cycles (Figure S6), which indicates that the pre-catalyst reached the steady state. *Ex situ* electrochemical impedance spectroscopy (EIS) results from the same electrode show that the charge transport resistance (R_{ct}) decreased significantly from 34 to 6.5 ohm (Ω), indicating faster charge transfer of CR-NiOOH (Figure 3B). To visualize the dynamic reconstruction process, the microstructures of intermediates at different stages were analyzed (Figures 3C–3F). After the first CV to 1.23 V_{RHE}, which is the equilibrium potential for OER, the surface of monocrystalline $NiMoO_4 \cdot xH_2O$ becomes amorphous (see Figure S7 for detailed characterization). After an anodic scan to 1.60 V_{RHE}, where the evolution of O_2 happens, the distinct three-layer region appears (Figure S8A). The outermost layer consists of ultrasmall low-crystalline NPs with an amorphous transitional interlayer and innermost $NiMoO_4 \cdot xH_2O$ layer. Because of the oxygen-evolving process, the surface Ni species are oxidized to OER-stable high-valence species. The generated (oxy)hydroxide is transformed *in situ* from surface species rather than by a dissolution-deposition process (Figure S9). Elemental distributions and content analyses depict the uniform distribution of Ni and O elements, whereas Mo shows a gradient distribution and decreases gradually from inner to outer (Figures S8D–S8F). When back at 0.924 V_{RHE} to achieve a complete CV cycle, the reconstruction degree deepens (Figure S10). A rough region with ~50-nm thickness is clearly visible in TEM images. Benefiting from the continuous co-leaching of crystal water and Mo species, $NiMoO_4 \cdot xH_2O$ is completely reconstructed only after 20-cycle CV. Based on the above results, the geometric/phase evolution is illustrated in Figures 3G–3J. Furthermore, the reconstruction mechanism is also proposed from the

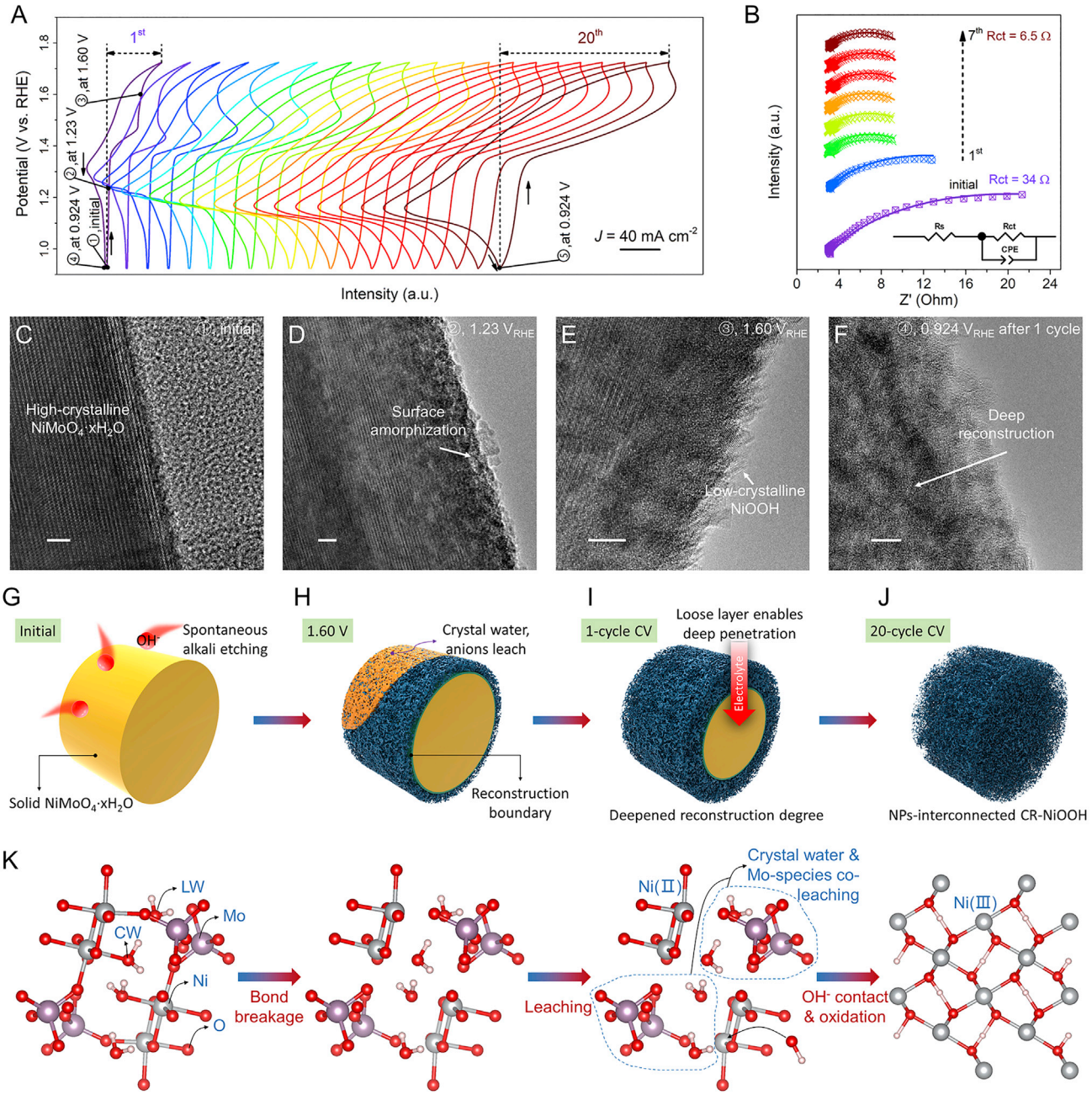

Figure 3. Dynamic Reconstruction Processes

(A) CV curves of $NiMoO_4 \cdot xH_2O$ NWs/NF measured at 0.924–1.724 V_{RHE} at 50 mV s^{-1}.

(B) *Ex situ* EIS spectra with fitting curves (solid lines) of $NiMoO_4 \cdot xH_2O$ NWs/NF at 1.524 V_{RHE}.

(C–F) *Ex situ* HRTEM images of $NiMoO_4 \cdot xH_2O$ at different stages during CV activation in (A). Scale bars, 5 nm.

(G–J) Schematic diagram of evolution, including the geometric/phase structure from the solid $NiMoO_4 \cdot xH_2O$ nanowire to the NP-interconnected NiOOH nanowire.

(K) Reconstruction process diagram from $NiMoO_4 \cdot xH_2O$ to NiOOH.

point of view of the crystal structure (Figure 3K). The reconstruction processes include bond breakage, co-leaching of crystal water and Mo species, and OH^- contact and electro-oxidation, which will be discussed further below.

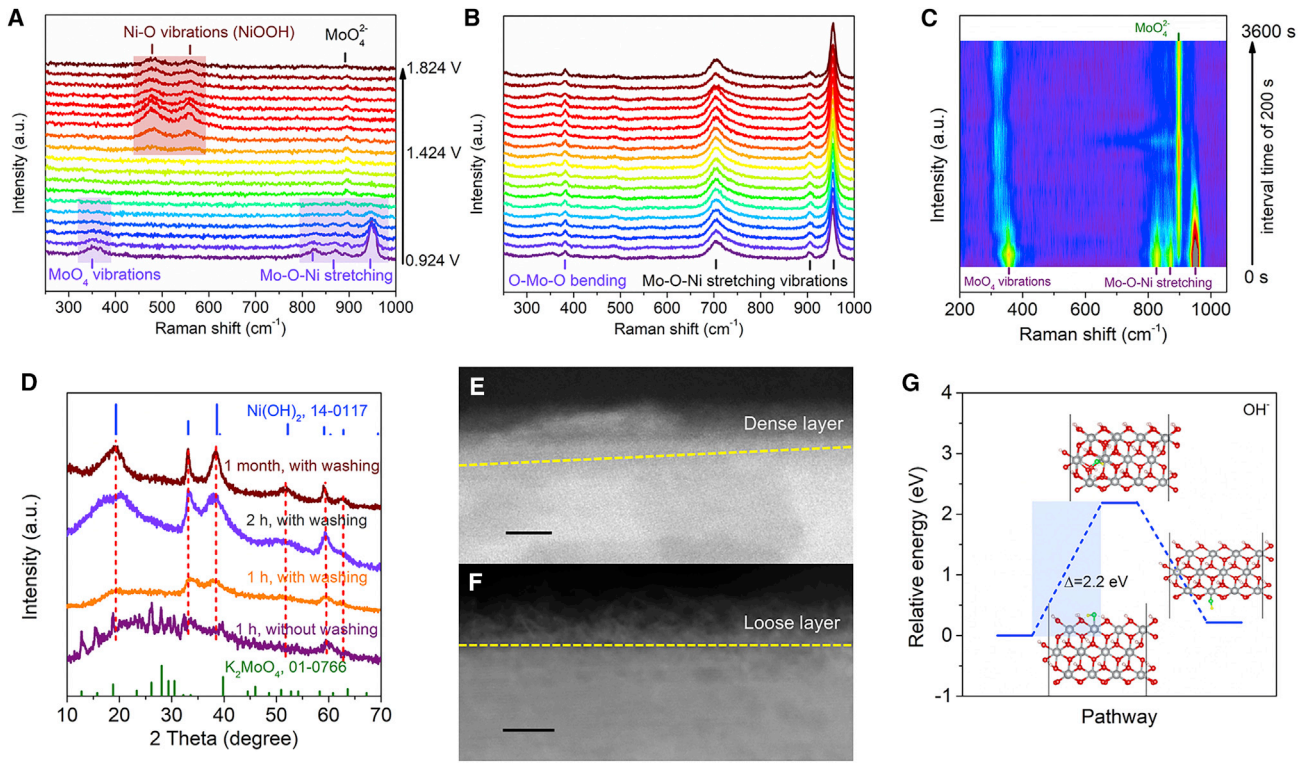

Figure 4. The Properties of the Reconstruction Layer Matter

(A and B) Potential-dependent *in situ* Raman spectra of (A) $NiMoO_4 \cdot xH_2O$ and (B) $NiMoO_4$ at 0.924–1.824 V_{RHE} with the interval voltage of 50 mV in 1 M KOH, showing that $NiMoO_4 \cdot xH_2O$ gradually reconstructs to CR-NiOOH but $NiMoO_4$ is almost unchanged.

(C) *In situ* Raman spectra of $NiMoO_4 \cdot xH_2O$ powder soaking in 1 M KOH with an interval time of 200 s.

(D) *Ex situ* XRD patterns of $NiMoO_4 \cdot xH_2O$ after soaking in 1 M KOH. The detected K_2MoO_4 and $Ni(OH)_2$ suggest the etching reaction ($NiMoO_4 \cdot xH_2O + 2OH^- \rightarrow Ni(OH)_2 + xH_2O + MoO_4^{2-}$).

(E and F) HAADF STEM images of (E) $NiMoO_4$ and (F) $NiMoO_4 \cdot xH_2O$ after soaking in KOH solution. Scale bars, 2 and 10 nm.

(G) DFT calculations of the relative energy for OH^-, which goes through NiOOH (101).

In Situ Capture of Intermediate States and the Formed Real Catalytic Species

In/ex situ technologies were further utilized to gain insights into the reconstruction mechanism of $NiMoO_4 \cdot xH_2O$. With the *ex situ* XRD measurement, disappearance of the representative peaks at ~27.3° and 29.8°, which belong to $NiMoO_4 \cdot xH_2O$, demonstrates its structural crack and amorphization (Figure S11A). An *in situ* electrochemistry-Raman coupling system was applied to understand electrocatalytic reactions in liquid electrolytes because of the high molecular specificity and non-interference of water of Raman signals.[26,27] At potentials below 1.324 V_{RHE}, the peak intensities of $NiMoO_4 \cdot xH_2O$ decrease with increased potential, indicating gradual destruction of its crystal structure (Figure 4A). At 1.424 V_{RHE}, two well-defined bands at 474 and 554 cm^{-1} appear that belong to NiOOH, and such a potential is attributed to the Ni(II)/Ni(III) oxidation peak (~1.37 V_{RHE}).[28] Here, the oxide phase forms below 1.424 V_{RHE}, which will be discussed later. The Raman peaks for NiOOH are kept as the applied bias voltage increases, indicating that it serves as an OER-stable catalytic species. Furthermore, the new peak at 900 cm^{-1} is assigned to MoO_4^{2-} in alkaline solution,[29] which originates from dissolution of Mo species. Contrary to $NiMoO_4 \cdot xH_2O$, $NiMoO_4$ shows unchanged Raman peaks under the same test conditions (Figure 4B). The undetected Raman peaks of NiOOH are attributed to its thin layer on the $NiMoO_4$ surface, as shown in Figure 2H.

The Properties of the Reconstruction Layer Matter

It should be noted that the reconstruction process for $NiMoO_4 \cdot xH_2O$ is complete and exhaustive rather than forming core-shell $NiMoO_4 \cdot xH_2O$@NiOOH as the final product. Generally, the reconstruction process is very common for the reported Ni-based OER catalysts. However, such a process is partial in these compounds, and only a thin layer of NiOOH/$Ni(OH)_2$ forms on their surface. Here the origins of the complete reconstruction of $NiMoO_4 \cdot xH_2O$ are analyzed. After soaking in 1 M KOH, $NiMoO_4 \cdot xH_2O$ was gradually etched by alkali. As shown in Figure 4C, the intensity of three Raman peaks at 800–1,000 cm^{-1} assigned to the Mo-O-Ni stretching vibration[30] decreases and almost disappears after soaking for 1 h, suggesting breakage of the Mo-O-Ni bond. The newly formed peak at 900 cm^{-1} is assigned to MoO_4^{2-}. The peak at 355 cm^{-1} assigned to MoO_4 vibration shifts to a lower wave number after soaking for 800 s, which may be associated with its vibrational environment. The Mo species are dissolved during reconstruction of $NiMoO_4 \cdot xH_2O$ (Figures S12A–S12C), and such a phenomenon also happens to the Ni-Mo nitride OER electrocatalyst reported by Yin et al..[25] The $NiMoO_4 \cdot xH_2O$ nanowire evolves to a nanosheet-assembled nanowire morphology after alkali etching (Figure S12D), and the etching reaction is further demonstrated by *ex situ* XRD patterns (Figure 4D). As a result, the washed product after soaking is $Ni(OH)_2$, whereas the K_2MoO_4 phase is detected for the product without washing. Therefore, when $NiMoO_4 \cdot xH_2O$ serves as pre-catalyst measured in 1 M KOH, the spontaneous etching reaction happens simultaneously. The multicomponent co-leaching results in a loose reconstruction layer and triggers its complete reconstruction.

As discussed above, the several-nanometer-thick reconstruction layer is observed for the $NiMoO_4$ pre-catalyst. Because the reconstruction reaction involves interaction with an alkaline solution, the limited reconstruction depth could be attributed to limited electrolyte penetration. A high-magnification STEM image of $NiMoO_4$ after soaking in 1 M KOH verifies our speculation because it shows the dense etching layer of ~3 nm (Figure 4E). However, for $NiMoO_4 \cdot xH_2O$, the fast etching rate makes the surface loose (Figure 4F), which facilitates electrolyte penetration for further etching. Therefore, we guess that the intrinsic properties of materials etched by alkali, which results in different etching structures, either loose or dense, are responsible for the two different results above. Even for the microns of Fe-doped cobalt molybdate hydrate, the loose etching structure enables its complete etching (Figure S13). It is not only difficult for alkaline solution to pass through the dense surface layer but also difficult for solution to pass through the crystal structure of the surface layer. Density functional theory (DFT) calculations confirm this difficulty by showing the high-energy barrier of 2.2 electron volt (eV) for OH^- to pass through the NiOOH layer (Figure 4G). Besides, for reported pre-catalysts such as Ni_2P[11] and Co_4N,[14] their post-OER products show the dense reconstruction layer, which supports our points.

Etching-Electrochemistry Co-Action versus Chemical Etching

CR catalysts feature an ultrasmall NPs-interconnected structure with evenly distributed gas-permeable pores, and the key is that etching and electro-oxidation reconstruction happen simultaneously. If $NiMoO_4 \cdot xH_2O$ is soaked in 1 M KOH prior to electro-oxidation, CR-NiOOH with a nanosheet-assembled nanowire structure can be obtained (Figures S14A and S4B, denoted CR-NiOOH*). This is because the etching reaction induces formation of monocrystalline/high-crystalline $Ni(OH)_2$ nanosheets (Figures S14C and S14D), which further evolve to (oxy)hydroxide during the subsequent electro-oxidation. Because the smaller-size catalyst is endowed with more exposed active sites, CR-NiOOH shows much better OER catalysis

(Figures S14E and S14F). $Ni(OH)_2$ nanosheet arrays grown on nickel foam were also prepared but with poor OER activity (Figure S15), suggesting the effectiveness of structure engineering for better catalysis. To explain the unique structure of CR-NiOOH, identifying the formed amorphous intermediates shown in Figure 3D is important. The voltage range below the theoretical decomposition voltage is analyzed, which is helpful for understanding the effects of voltage bias during alkali etching. After CV at 0.924–1.224 V_{RHE}, the nanowires mainly consist of ~5-nm polycrystalline NiO NPs (Figure S16F). Furthermore, the Raman peak at 460 cm^{-1} is assigned to the Ni-O stretching mode of NiO, and other peaks may be assigned to molybdenum oxides, indicating phase separation and formation of amorphous oxide intermediates (Figures S16G and S16H). These results suggest that the simultaneous etching-reconstruction processes facilitate formation of an ultrasmall NP-interconnected structure with nanopores.

The prerequisites for forming ultrasmall NP-interconnected CR catalysts can be summarized as follows: (1) achieving complete collapse of bulk materials, (2) promoting deep penetration of electrolytes for inner electro-oxidation as the loose reconstruction layer dominates, and (3) simultaneous reconstruction and etching. To demonstrate the universality of these results, other bulk alkali-sensitive pre-catalysts, such as $NiMoO_4 \cdot xH_2O$ nanosheets, Ni-BTC (BTC = 1,3,5-benzene tricarboxylate) metal organic framework microspheres, $CoMoO_4 \cdot 0.75H_2O$ nanowires, and $Co(CO_3)_{0.5}(OH) \cdot 0.11H_2O$ nanowires, were also investigated (Figure S17). All of them can completely evolve to their corresponding hydroxides after alkali etching, which guarantees complete reconstruction of CR catalysts. Consequently, the CR catalysts of the (oxy)hydroxide phase are obtained with the ultrasmall NP-interconnected multilevel structure. Therefore, the complete reconstruction mechanism can be widely extended to various bulk alkali-sensitive pre-catalysts.

Ultrastable Catalysis in Alkali

Using a standard three-electrode system, $NiMoO_4 \cdot xH_2O$ NWs/NF was directly employed as a binder-free working electrode to achieve activation and acquire the (oxy) hydroxide arrays. Before performance evaluation, the purity of KOH solution was examined. KOH reagent purity (Fe content of < 0.001%) and undetected Fe 2p XPS signals using an Mg source confirmed the absence of Fe impurities in the solution used.[19] CV curves of $NiMoO_4 \cdot xH_2O$ ink coated on the carbon cloth for the initial cycles are provided in Figure 5A. The small shift (~20 mV) of the Ni(II)/Ni(III) oxidation peak is much below 50 mV, negating the influence of iron according to Klaus et al.[31] The chronopotentiometric response of fresh $NiMoO_4 \cdot xH_2O$ shows a gradually decreased potential, but the potentials of $NiMoO_4$ are almost unchanged, indicating fast reconstruction on the $NiMoO_4 \cdot xH_2O$ surface during activation (Figure S18A). The simplex nickel foam shows the increased potentials, implying that the activity enhancement of $NiMoO_4 \cdot xH_2O$ is independent of the substrate. After activation, the obtained CR-NiOOH was tested in 1 M Fe-free KOH, whereas surface-reconstructed $NiMoO_4$@NiOOH and commercial IrO_2/C served as control samples. Linear sweep voltammetry (LSV) curves were normalized by geometric area, electrochemically active surface area (ECSA), and catalyst mass, respectively (Figures S18B–S18D). CR-NiOOH has much higher OER activity than $NiMoO_4$@NiOOH. For example, CR-NiOOH requires the lowest overpotential at 10 mA cm^{-2} (η_{10} of 278.2 mV), which is much lower than that of $NiMoO_4$@NiOOH (353.6 mV). To reveal the advantages of the CR catalyst for the OER, the mass activity-related overpotential $\eta_{10,\,m}$ ($\eta_{10,\,m}$ is calculated as the ratio of η_{10} and mass of the loading catalysts) is compared. The $\eta_{10,\,m}$ of CR-NiOOH (289 mV mg^{-1}) is even lower than that of the commercial IrO_2/C (325.9 mV mg^{-1}), indicating that it can serve as a superior

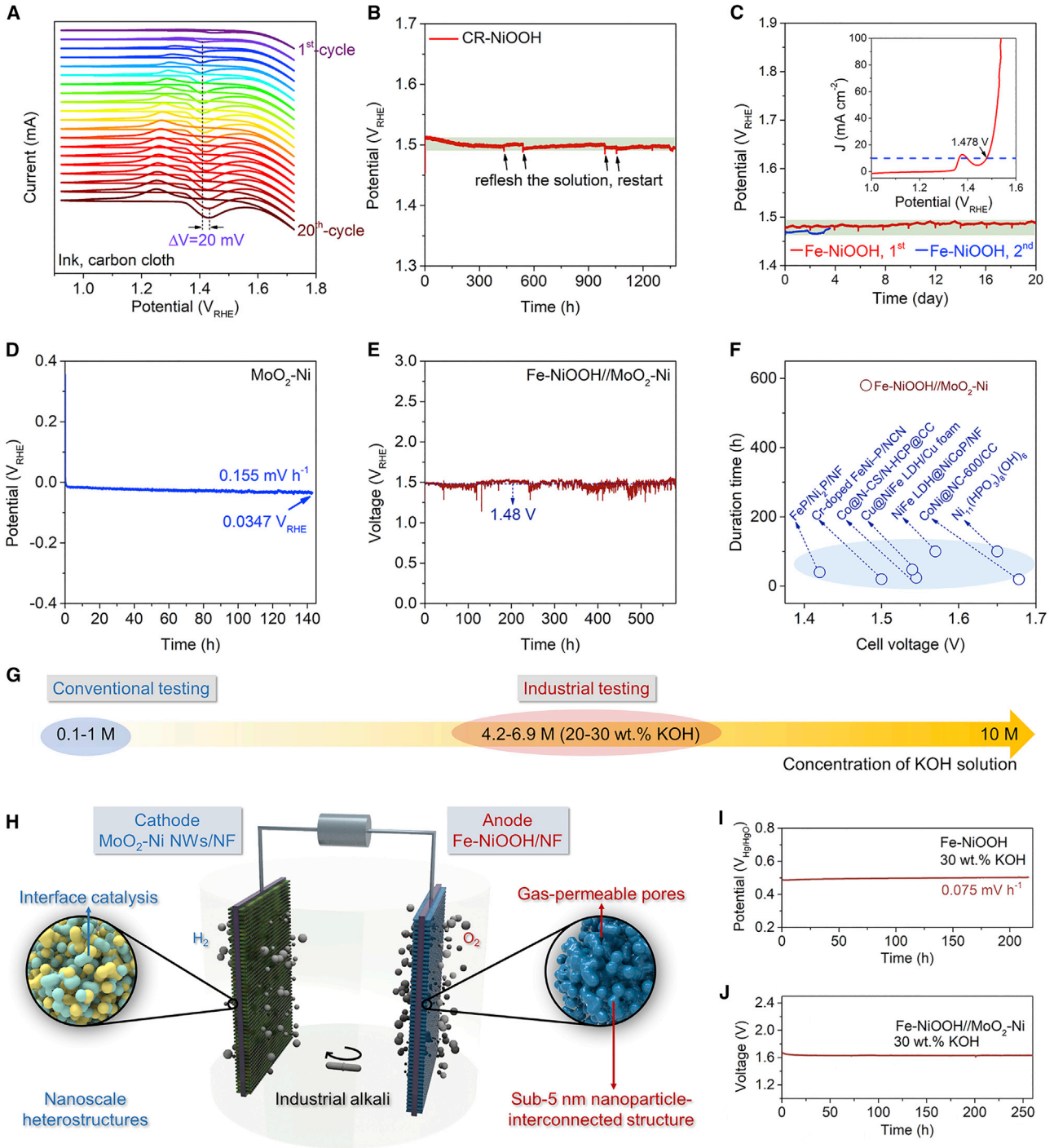

Figure 5. Catalytic Performance

(A) CV curves of $NiMoO_4 \cdot xH_2O$ ink coated on the carbon cloth at 0.924–1.724 V_{RHE} at 50 mV s^{-1}.

(B) Chronopotentiometric measurement of CR-NiOOH at 10 mA cm^{-2} in 1 M KOH.

(C) Chronopotentiometric measurements of Fe-NiOOH at 10 mA cm^{-2} in 1 M KOH. Inset: iR-compensated polarization curve of Fe-NiOOH normalized by a geometric area of nickel foam.

(D) Chronopotentiometric measurement of $NiMoO_4 \cdot xH_2O$-derived heterostructured MoO_2-Ni arrays at −10 mA cm^{-2} in 1 M KOH for HER.

(E) Water electrolysis performance at 10 mA cm^{-2} in 1 M KOH.

(F) Comparison of recently reported AWE performances based on coupled (or bifunctional) catalysts tested in 1 M KOH.

catalyst. However, the $\eta_{10,\,m}$ value of $NiMoO_4$@NiOOH is as high as 393.2 mV mg^{-1}. In addition to a high-mass-activity OER, the CR catalyst also possesses the advantage of 97.4% Faradaic efficiency (Figure S18E). The 2.6% loss may be due to the dissolved gas in the solution and gas adsorbed on the electrode.[32]

The reasons why CR-NiOOH is superior to $NiMoO_4$@NiOOH were analyzed. First, CR-NiOOH possesses more OER-active species, whereas an ~7-nm-thin layer of NiOOH on $NiMoO_4$ serves as a catalytic species; thus, the former can achieve a higher mass activity toward surface-catalyzed reactions. Our as-prepared NiOOH is reconstructed completely and *in situ* from $NiMoO_4 \cdot xH_2O$, and the whole catalyst could perform the catalytic reactions with abundant catalytic sites. The higher intensity of the oxidation peak at ~1.37 V for CR-NiOOH (Figures S18B–S18D) suggests larger amounts of active phases as well.[21] Second, CR-NiOOH possesses a sub-5-nm NP-interconnected structure. This unique multilevel structure is endowed with numerous pores accessible to electrolytes and conductive to gas diffusion. Although NiOOH has been shown to not be very active in the OER,[31] the low-crystalline characteristics and abundant defects in catalysts have been reported to accelerate the OER kinetics.[33] Therefore, the newly developed CR-NiOOH shows great potential as an IrO_2-substituted oxygen evolving system. More importantly, CR-NiOOH exhibits a negligible change in potential after 1,350 h in the durability test, which demonstrates its potential for ultrastable electrolytic applications (Figure 5B). Electron microscope characterization after the durability test displayed an unchanged morphology and retained microstructure, suggesting a robust and stable nature of NiOOH in the face of corrosion (Figure S19). Its excellent stability is mainly attributed to the robust (oxy)hydroxide NP-interconnected structure with evenly distributed gas-permeable pores. To show the multiple applications of CR-NiOOH, the urea oxidation reaction (UOR) was also measured, which is essential for urea electrolysis and also has sluggish kinetics.[34] As a result, it shows decreased overpotential of 106 mV at 10 mA mg^{-1} compared with that of $NiMoO_4$@NiOOH and good durability for 110 h at 0.48 $V_{Hg/HgO}$ (Figure S20). In addition, CR-NiOOH can also provide stable OER catalysis at a high temperature of 52.4°C for 120 h, with an overpotential increase of only ~10 mV (Figure S21).

Fe impurities in the testing solution greatly enhance the OER activity of NiOOH,[35] which is attributed to formation of highly active nickel-iron (oxy)hydroxide. Here, the advanced iron-incorporated nickel (oxy)hydroxide (denoted Fe-NiOOH) was fabricated *in situ* in 1 M KOH solution containing a trace of Fe by adding an iron source. To achieve 10 mg cm^{-2}, a small overpotential of 248 mV is required (inset in Figure 5C). The enhanced OER catalysis is attributed to its electronic tuning by Fe incorporation and enhanced electron conductivity. During a 20-day long-term chronopotentiometry measurement of Fe-NiOOH, the potential is almost unchanged, with a small potential change of only 10 mV (Figure 5C). These results confirm the well-retained ultrastable property after optimizing its electronic structure. To demonstrate the water electrolysis application, our reported heterostructured MoO_2-Ni NWs/NF were chosen as hydrogen evolution reaction (HER) electrodes.[36] As shown in Figure 5D, the MoO_2-Ni NWs/NF featured by interface catalysis exhibits excellent HER activity with a small decay of 0.155 mV h^{-1}. When pairing Fe-NiOOH with MoO_2-Ni arrays in a two-electrode alkaline water

(G) Conventional test conditions (almost in 0.1–1 M KOH) in most reports have a certain gap with the industrial-concentration one (in 4.2–6.9 M KOH).
(H) Schematic diagram of the water electrolyzer using MoO_2-Ni and Fe-NiOOH electrodes.
(I) Chronopotentiometric measurement of Fe-NiOOH at 10 mA cm^{-2} in 30 wt % KOH.
(J) AWE performance at 10 mA cm^{-2} in 30 wt % KOH.

electrolyzer, the electrolyzer delivers 10 mA cm^{-2} at 1.48 V for over 580 h under fast-moving fluid condition produced by rapid stirring of fresh magneton (Figure 5E). Its electrolysis durability is superior to that in previous reports (Figure 5F; Table S3). These results highlight the potential of CR catalysts for ultrastable and high-efficiency catalytic applications.

Most industrial alkaline electrolyzers are operated in a strong alkaline KOH solution (>20 wt %; Figure 5G). Therefore, we evaluated the half-reaction catalysis and AWE performance based on the abovementioned array system in a two-electrode cell in 30 wt % KOH, as illustrated schematically in Figure 5H. Under such harsh operating conditions, the Fe-NiOOH anode still performs stable OER catalysis at ~0.5 $V_{Hg/HgO}$ for over 210 h with activity decay of 0.075 mV h^{-1} (Figure 5I). Fe-NiOOH maintains its structural and component characterization after testing under such harsh conditions (Figure S22). For the cathodic MoO_2-Ni array, it can catalyze HER for 300 h with activity decay of 0.21 mV h^{-1} (Figure S23). Here, the 10 μL solution containing 0.6 mg $Fe(NO_3)_3 \cdot 9H_2O$ was also added to ensure the same test environment as for OER testing. As expected, the Fe-NiOOH//MoO_2-Ni array system operated for 260 h (Figure 5J), indicating its potential practical applications. Performance evaluation of reported catalysts in industrial-concentration alkali has also been provided for comparison (Table S4).

For the $NiMoO_4$ pre-catalyst, the alkali etching rate on its surface is slow in 1 M KOH, and a dense reconstruction layer forms via surface reconstruction. This leads to quick termination of reconstruction. However, under harsh conditions of 30 wt % KOH, alkali etching is accelerated, and leaching of Mo species is promoted. This could result in a porous structure of the reconstruction layer and promote deep reconstruction in concurrent electro-oxidation processes. Therefore, $NiMoO_4$ can also be completely reconstructed to (oxy)hydroxide in 30 wt % KOH, which is reflected by decreased potentials because of the enhanced number of active species (Figure S24). This result suggests that some pre-catalysts (such as phosphides, nitrides, and chalcogenides) may also be completely reconstructed to stable catalytic species in industrial alkali. Therefore, understanding reconstruction chemistry and evaluating performance under realistic conditions are necessary and meaningful, especially for pre-catalysts involved in reconstruction.

In summary, we discovered different reconstruction results for hydrate/anhydrous molybdate pre-catalysts at oxidized potentials in 1 M KOH; i.e., complete/surface reconstruction. Such a difference depends on the microstructure characteristics (dense or loose) of the reconstructed layer, caused by different leaching species from pre-catalysts. The proposed reconstruction mechanism can be extended to other bulk alkali-sensitive pre-catalysts, resulting in a series of electrochemically formed CR catalysts. These CR catalysts display a unique structure interconnected by ultrasmall NPs endowed with abundant defects and pores accessible to electrolytes. Such an interconnected structure allows CR-NiOOH to perform ultrastable catalysis for 1,350 h. After iron incorporation, the obtained Fe-NiOOH exhibits remained structure and ultrastable catalysis. The coupled Fe-NiOOH and MoO_2-Ni system was confirmed with excellent water electrolysis performance in 1 M and 30 wt % KOH. Furthermore, different reconstruction results of anhydrous $NiMoO_4$ in industrial alkali were obtained, suggesting the importance of evaluating catalysts under realistic conditions. This work highlights fundamental reconstruction chemistry, CR catalysts with a unique structure and ultrastable catalytic properties, and different reconstruction phenomena in low-concentration and industrial alkali.

EXPERIMENTAL PROCEDURES

Resource Availability

Lead Contact

Requests for further information and resources and reagents can be directed to the Lead Contact, Prof. Liqiang Mai (mlq518@whut.edu.cn).

Materials Availability

This study did not generate new unique reagents.

Data and Code Availability

The authors declare that the data supporting the findings of this study are available within the article and the Supplemental Information. All other data are available from the Lead Contact upon reasonable request.

Synthesis of CR-NiOOH Nanowire/Nanosheet Arrays and $NiMoO_4$ Nanowire Arrays

First, $NiMoO_4 \cdot xH_2O$ nanowire/nanosheet arrays on nickel foam were fabricated following previous reports.[36,37] Next, the anodic oxidation process on $NiMoO_4 \cdot xH_2O$ precursor was carried out in the standard three-electrode system in 1 M KOH and operated on an CHI760E electrochemical analyzer. A piece of $NiMoO_4 \cdot xH_2O$ served as a working electrode, and the graphite rod and the unused Hg/HgO electrode served as a counterelectrode and a reference electrode, respectively. After carrying out CV tests in 0.924–1.724 V_{RHE} at a scan rate of 50 mV s^{-1} for 30 cycles, black CR-NiOOH nanowire/nanosheet arrays were obtained with a mass loading of ~1.2 mg cm^{-2}. In addition, after calcination of $NiMoO_4 \cdot xH_2O$ nanowire arrays at 550°C, $NiMoO_4$ nanowire arrays with a mass loading of ~2.6 mg cm^{-2} were fabricated.

Scalable Synthesis of $NiMoO_4 \cdot xH_2O$ Arrays

24 mmol $Ni(NO_3)_2 \cdot 6H_2O$ and 24 mmol $Na_2MoO_4 \cdot 2H_2O$ were dissolved into 360 mL deionized water and formed a transparent green solution. The solution was then transferred into a 500-mL Teflon-lined autoclave, and four pieces of nickel foam were added. After reaction at 120°C for 6 h, the nickel foam samples were taken out, washed, and vacuum dried, and $NiMoO_4 \cdot xH_2O$ arrays were obtained.

Synthesis of CoOOH Derived from $CoMoO_4 \cdot 0.75H_2O$ and $Co(CO_3)_{0.5}(OH) \cdot 0.11H_2O$ Nanowires and NiOOH Microspheres Derived from Ni-BTC Microspheres

First, $CoMoO_4 \cdot 0.75H_2O$ nanowires,[38] $Co(CO_3)_{0.5}(OH) \cdot 0.11H_2O$ nanowires,[39] and Ni-BTC microspheres[40] were fabricated according to previous reports. Next, these compounds were transformed into the corresponding CR catalysts after CV activation at 0.924–1.724 V_{RHE} at 50 mV s^{-1} for more than 30 cycles.

Material Characterization

Scanning electron microscope (SEM) images were collected with a JEOL-7100F microscope at an acceleration voltage range of 15–25 kV. Microscopy images, SAED patterns, elemental mapping, and linear scanning analysis were collected on JEM-2100F and Thermo Fisher Scientific Titan G260-300 scanning/transmission electron microscopes. *Ex situ* XRD patterns were obtained using a Bruker D8 Advance X-ray diffractometer with Cu Kα radiation. *In situ* XRD patterns for alkali soaking experiments were recorded using a Bruker D2 Phaser X-ray diffractometer. Raman spectra and *in situ* Raman spectra for alkali soaking experiments were recorded using a HORIBA HR EVO Raman system. XPS measurements were carried out using an

ESCALAB 250Xi instrument. Element content was determined using an inductively coupled plasma atomic emission spectrometer (ICP-AES) on a PerkinElmer Optima 4300DV spectrometer.

Electrochemical Measurements

All electrochemical measurements were carried out in fresh KOH (1 M or 30 wt %) on a CHI 760E electrochemical station using a standard three-electrode system. The test samples grown on the substrates (nickel foam or carbon cloth) served as a working electrode, and an unused Hg/HgO electrode was applied as a reference electrode; a graphite rod served as a counterelectrode. EIS was recorded in a frequency range of 0.01–100,000 Hz. Homogeneous ink was prepared by dispersing 8 mg commercial IrO_2/C and 2 mg Vulcan XC-72R in 250 μL deionized water, 700 μL isopropyl alcohol, and 50 μL Nafion solution (5 wt %). Next, 9 μL ink was coated on glassy carbon with an area of 0.07069 cm^2 for catalytic tests. All chronopotentiometric measurements were carried out by applying a constant current density of 10 mA cm^{-2}. In 1 M KOH, the iR-corrected potentials were referenced to RHE based on the following equation:

$$E_{RHE} = E_{Hg/HgO} + 0.059 \times pH + E^{o}_{Hg/HgO} - iR.$$

In situ electrochemistry-Raman measurements were recorded using a HORIBA HR EVO Raman system (633 nm laser) and an electrochemical workstation (CHI760E). The potential-dependent *in situ* Raman spectra were recorded with 150-s duration and a 50-s interval, and the LSV measurements were carried out in 0.924–1.824 V_{RHE} at 0.25 mV s^{-1} in 1 M KOH during *in situ* Raman testing. Time-dependent *in situ* Raman spectra were recorded at 10 mA cm^{-2} with an interval time of 150 s.

Computational Details

All DFT simulations were performed using Vienna *ab initio* simulation package (VASP) software.[41] The exchange-correlation interactions were described by generalized gradient approximation (GGA)[42] within the Perdew-Burke-Ernzerhof (PBE) function.[43] A plane wave basis set was adopted with a cutoff of 500 eV. Gaussian-type smearing with an energy window of 0.05 eV was used for optimization and frequency calculation. The energy convergence tolerance was 0.01 milli-electron volt (meV). The force tolerance for the optimization task was 0.05 eV/Å. All calculations were performed with spin unrestricted, and initial magnetic moments of 2 Bohr magneton (μ_B) for Ni, 1 μ_B for K, and 0 μ_B for O and H were set. 1 × 1 × 1 K point was sampled. The GGA with Hubbard U parameter (GGA+U) method for Ni species was adopted with an Hubbard effective parameter (U-J) value of 6.6 eV, the same as in previous reports.[44] The DFT-D3 method was adopted for all calculations. The linear mixing parameter was set to 0.06, and the cutoff wave vector for the Kerker mixing scheme was set to 0.0001 to make electron state converge more stable than default settings.

SUPPLEMENTAL INFORMATION

Supplemental Information can be found online at https://doi.org/10.1016/j.xcrp.2020.100241.

ACKNOWLEDGMENTS

This work was supported by the National Natural Science Foundation of China (51521001 and 21890751), the National Key Research and Development Program of China (2016YFA0202603), the National Innovation and Entrepreneurship Training Program for College Students (WUT: 20191049701034), and the Foshan Xianhu

Laboratory of the Advanced Energy Science and Technology Guangdong Laboratory (XHT2020-003). The S/TEM work was performed at the Nanostructure Research Center (NRC), supported by the Fundamental Research Funds for the Central Universities (WUT: 2019III012GX and 2020III002GX).

AUTHOR CONTRIBUTIONS

X. Liu and L.M. conceived the idea. X. Liu, J.M., L.M., and R.G. designed the experiments, analyzed the results, and wrote the manuscript. X. Liu, B.W., and R.G. performed the experiments and analyzed the results. X. Liu, K.N., and X.W. performed the DFT computations and theoretical analyses. D.Z., J.W., and L.M. provided helpful suggestions and refined the manuscript. All authors read and commented on the manuscript and approved the final version of the manuscript.

DECLARATION OF INTERESTS

A patent application related to this work has been submitted in China (application number 201811648828.2).

Received: July 18, 2020
Revised: September 4, 2020
Accepted: September 29, 2020
Published: November 4, 2020

REFERENCES

1. Park, S., Shao, Y.Y., Liu, J., and Wang, Y. (2012). Oxygen electrocatalysts for water electrolyzers, and reversible fuel cells: status, and perspective. Energy Environ. Sci. *5*, 9331–9344.

2. Li, Y.G., Gong, M., Liang, Y.Y., Feng, J., Kim, J.-E., Wang, H.L., Hong, G.S., Zhang, B., and Dai, H.J. (2013). Advanced zinc-air batteries based on high-performance hybrid electrocatalysts. Nat. Commun. *4*, 1805.

3. Hua, B., Li, M., Pang, W.Y., Tang, W.Q., Zhao, S.L., Jin, Z.H., Zeng, Y.M., Amirkhiz, B.S., and Luo, J.-L. (2018). Activating p-blocking centers in perovskite for efficient water splitting. Chem *4*, 2902–2916.

4. Trotochaud, L., Young, S.L., Ranney, J.K., and Boettcher, S.W. (2014). Nickel-iron oxyhydroxide oxygen-evolution electrocatalysts: the role of intentional and incidental iron incorporation. J. Am. Chem. Soc. *136*, 6744–6753.

5. McCrory, C.C.L., Jung, S., Peters, J.C., and Jaramillo, T.F. (2013). Benchmarking heterogeneous electrocatalysts for the oxygen evolution reaction. J. Am. Chem. Soc. *135*, 16977–16987.

6. Jiao, Y., Zheng, Y., Jaroniec, M., and Qiao, S.Z. (2015). Design of electrocatalysts for oxygen- and hydrogen-involving energy conversion reactions. Chem. Soc. Rev. *44*, 2060–2086.

7. Wu, T.Z., Sun, S.N., Song, J.J., Xi, S.B., Du, Y.H., Chen, B., Sasangka, W.A., Liao, H.B., Gan, C.L., Scherer, G.G., et al. (2019). Iron-facilitated dynamic active-site generation on spinel $CoAl_2O_4$ with self-termination of surface reconstruction for water oxidation. Nat. Catal. *2*, 763–772.

8. Liu, X., Guo, R.T., Ni, K., Xia, F.J., Niu, C.J., Wen, B., Meng, J.S., Wu, P.J., Wu, J.S., Wu, X.J., and Mai, L.Q. (2020). Reconstruction-determined alkaline water electrolysis at industrial temperatures. Adv. Mater. *32*, e2001136.

9. Fabbri, E., Nachtegaal, M., Binninger, T., Cheng, X., Kim, B.-J., Durst, J., Bozza, F., Graule, T., Schäublin, R., Wiles, L., et al. (2017). Dynamic surface self-reconstruction is the key of highly active perovskite nano-electrocatalysts for water splitting. Nat. Mater. *16*, 925–931.

10. Jiang, H.L., He, Q., Zhang, Y.K., and Song, L. (2018). Structural self-reconstruction of catalysts in electrocatalysis. Acc. Chem. Res. *51*, 2968–2977.

11. Stern, L.-A., Feng, L.G., Song, F., and Hu, X.L. (2015). Ni_2P as a Janus catalyst for water splitting: the oxygen evolution activity of Ni_2P nanoparticles. Energy Environ. Sci. *8*, 2347–2351.

12. Zou, X.X., Wu, Y.Y., Liu, Y.P., Liu, D.P., Li, W., Gu, L., Liu, H., Wang, P.W., Sun, L., and Zhang, Y. (2018). In Situ generation of bifunctional, efficient Fe-based catalysts from mackinawite iron sulfide for water splitting. Chem *4*, 1139–1152.

13. Jin, S. (2017). Are metal chalcogenides, nitrides, and phosphides oxygen evolution catalysts or bifunctional catalysts? ACS Energy Lett. *2*, 1937–1938.

14. Chen, P.Z., Xu, K., Fang, Z.W., Tong, Y., Wu, J.C., Lu, X.L., Peng, X., Ding, H., Wu, C.Z., and Xie, Y. (2015). Metallic Co_4N porous nanowire arrays activated by surface oxidation as electrocatalysts for the oxygen evolution reaction. Angew. Chem. Int. Ed. Engl. *54*, 14710–14714.

15. Grimaud, A., Demortiere, A., Saubanere, M., Dachraoui, W., Duchamp, M., Doublet, M.-L., and Tarascon, J.-M. (2017). Activation of surface oxygen sites on an iridium-based model catalyst for the oxygen evolution reaction. Nat. Energy *2*, 17002.

16. Roy, C., Sebok, B., Scott, S.B., Fiordaliso, E.M., Sørensen, J.E., Bodin, A., Trimarco, D.B., Damsgaard, C.D., Vesborg, P.C.K., Hansen, O., et al. (2018). Impact of nanoparticle size and lattice oxygen on water oxidation on $NiFeO_xH_y$. Nat. Catal. *1*, 820–829.

17. Zhang, B.W., Jiang, K., Wang, H.T., and Hu, S. (2019). Fluoride-induced dynamic surface self-reconstruction produces unexpectedly efficient oxygen-evolution catalyst. Nano Lett. *19*, 530–537.

18. Jiang, H.L., He, Q., Li, X.Y., Su, X.Z., Zhang, Y.K., Chen, S.M., Zhang, S., Zhang, G.Z., Jiang, J., Luo, Y., et al. (2019). Tracking structural self-reconstruction and identifying true active sites toward cobalt oxychloride precatalyst of oxygen evolution reaction. Adv. Mater. *31*, e1805127.

19. Liu, X., Ni, K., Wen, B., Guo, R.T., Niu, C.J., Meng, J.S., Li, Q., Wu, P.J., Zhu, Y.W., Wu, X.J., and Mai, L.Q. (2019). Deep reconstruction of nickel-based precatalysts for water oxidation catalysis. ACS Energy Lett. *4*, 2585–2592.

20. Su, X.Z., Wang, Y., Zhou, J., Gu, S.Q., Li, J., and Zhang, S. (2018). Operando spectroscopic identification of active sites in NiFe prussian blue analogues as electrocatalysts: activation of oxygen atoms for oxygen evolution reaction. J. Am. Chem. Soc. *140*, 11286–11292.

21. Yan, Z.H., Sun, H.M., Chen, X., Liu, H.H., Zhao, Y.R., Li, H.X., Xie, W., Cheng, F.Y., and Chen, J. (2018). Anion insertion enhanced electrodeposition of robust metal hydroxide/oxide electrodes for oxygen evolution. Nat. Commun. *9*, 2373.

22. Zeng, K., and Zhang, D.K. (2010). Recent progress in alkaline water electrolysis for hydrogen production and applications. Progr. Energy Combust. Sci. *36*, 307–326.

23. Eda, K., Uno, Y., Nagai, N., Sotani, N., and Whittingham, M.S. (2005). Crystal structure of cobalt molybdate hydrate $CoMoO_4 \cdot nH_2O$. J. Solid State Chem. *178*, 2791–2797.

24. Jiang, J., Sun, F.F., Zhou, S., Hu, W., Zhang, H., Dong, J.C., Jiang, Z., Zhao, J.J., Li, J.F., Yan, W.S., and Wang, M. (2018). Atomic-level insight into super-efficient electrocatalytic oxygen evolution on iron and vanadium co-doped nickel (oxy)hydroxide. Nat. Commun. *9*, 2885.

25. Yin, Z.X., Sun, Y., Zhu, C.L., Li, C.Y., Zhang, X.T., and Chen, Y.J. (2017). Bimetallic Ni-Mo nitride nanotubes as highly active and stable bifunctional electrocatalysts for full water splitting. J. Mater. Chem. A Mater. Energy Sustain. *5*, 13648–13658.

26. Faisal, F., Stumm, C., Bertram, M., Waidhas, F., Lykhach, Y., Cherevko, S., Xiang, F.F., Ammon, M., Vorokhta, M., Šmíd, B., et al. (2018). Electrifying model catalysts for understanding electrocatalytic reactions in liquid electrolytes. Nat. Mater. *17*, 592–598.

27. Zhu, K.Y., Zhu, X.F., and Yang, W.S. (2019). Application of in situ techniques for the characterization of NiFe-based oxygen evolution reaction (OER) electrocatalysts. Angew. Chem. Int. Ed. Engl. *58*, 1252–1265.

28. Wang, J., Gan, L.Y., Zhang, W.Y., Peng, Y.C., Yu, H., Yan, Q.Y., Xia, X.H., and Wang, X. (2018). In situ formation of molecular Ni-Fe active sites on heteroatom-doped graphene as a heterogeneous electrocatalyst toward oxygen evolution. Sci. Adv. *4*, eaap7970.

29. Himeno, S., Niiya, H., and Ueda, T. (1997). Raman studies on the identification of isopolymolybdates in aqueous solution. Bull. Chem. Soc. Jpn. *70*, 631–637.

30. Zhang, Z., Liu, Y.D., Huang, Z.Y., Ren, L., Qi, X., Wei, X.L., and Zhong, J.X. (2015). Facile hydrothermal synthesis of $NiMoO_4$@$CoMoO_4$ hierarchical nanospheres for supercapacitor applications. Phys. Chem. Chem. Phys. *17*, 20795–20804.

31. Klaus, S., Cai, Y., Louie, M.W., Trotochaud, L., and Bell, A.T. (2015). Effects of Fe electrolyte impurities on $Ni(OH)_2$/NiOOH structure and oxygen evolution activity. J. Phys. Chem. C *119*, 7243–7254.

32. Wang, J., Li, K., Zhong, H.-X., Xu, D., Wang, Z.-L., Jiang, Z., Wu, Z.-J., and Zhang, X.-B. (2015). Synergistic effect between metal-nitrogen-carbon sheets and NiO nanoparticles for enhanced electrochemical water-oxidation performance. Angew. Chem. Int. Ed. Engl. *54*, 10530–10534.

33. Li, J.T., Huang, W.Z., Wang, M.M., Xi, S.B., Meng, J.S., Zhao, K.N., Jin, J., Xu, W.W., Wang, Z.Y., Liu, X., et al. (2019). Low-crystalline bimetallic metal-organic framework electrocatalysts with rich active sites for oxygen evolution. ACS Energy Lett. *4*, 285–292.

34. Yu, Z.-Y., Lang, C.-C., Gao, M.-R., Chen, Y., Fu, Q.-Q., Duan, Y., and Yu, S.-H. (2018). Ni-Mo-O nanorod-derived composite catalysts for efficient alkaline water-to-hydrogen conversion via urea electrolysis. Energy Environ. Sci. *11*, 1890–1897.

35. Stevens, M.B., Trang, C.D.M., Enman, L.J., Deng, J., and Boettcher, S.W. (2017). Reactive Fe-sites in Ni/Fe (oxy)hydroxide are responsible for exceptional oxygen electrocatalysis activity. J. Am. Chem. Soc. *139*, 11361–11364.

36. Liu, X., Ni, K., Niu, C.J., Guo, R.T., Xi, W., Wang, Z.Y., Meng, J.S., Li, J.T., Zhu, Y.W., Wu, P.J., et al. (2019). Upraising the O 2p orbital by integrating Ni with MoO_2 for accelerating hydrogen evolution kinetics. ACS Catal. *9*, 2275–2285.

37. Peng, S.J., Li, L.L., Wu, H.B., Madhavi, S., and Lou, X.W. (2015). Controlled growth of $NiMoO_4$ nanosheet and nanorod arrays on various conductive substrates as advanced electrodes for asymmetric supercapacitors. Adv. Energy Mater. *5*, 1401172.

38. Mandal, M., Ghosh, D., Giri, S., Shakir, I., and Das, C.K. (2014). Polyaniline-wrapped 1D $CoMoO_4 \cdot 0.75H_2O$ nanorods as electrode materials for supercapacitor energy storage applications. RSC Advances *4*, 30832–30839.

39. Zhu, L.P., Wen, Z., Mei, W.M., Li, Y.G., and Ye, Z.Z. (2013). Porous CoO nanostructure arrays converted from rhombic Co(OH)F and needle-like $Co(CO_3)_{0.5}(OH) \cdot 0.11H_2O$ and their electrochemical properties. J. Phys. Chem. C *117*, 20465–20473.

40. Zou, F., Chen, Y.-M., Liu, K.W., Yu, Z.T., Liang, W.F., Bhaway, S.M., Gao, M., and Zhu, Y. (2016). Metal organic frameworks derived hierarchical hollow NiO/Ni/graphene composites for lithium and sodium storage. ACS Nano *10*, 377–386.

41. Hafner, J. (2008). Ab-initio simulations of materials using VASP: Density-functional theory and beyond. J. Comput. Chem. *29*, 2044–2078.

42. Perdew, J.P., Burke, K., and Ernzerhof, M. (1996). Generalized gradient approximation made simple. Phys. Rev. Lett. *77*, 3865–3868.

43. Ernzerhof, M., and Scuseria, G.E. (1999). Assessment of the Perdew-Burke-Ernzerh of exchange-correlation functional. J. Chem. Phys. *110*, 5029–5036.

44. Friebel, D., Louie, M.W., Bajdich, M., Sanwald, K.E., Cai, Y., Wise, A.M., Cheng, M.-J., Sokaras, D., Weng, T.-C., Alonso-Mori, R., et al. (2015). Identification of highly active Fe sites in (Ni,Fe)OOH for electrocatalytic water splitting. J. Am. Chem. Soc. *137*, 1305–1313.